

Technical Note

Multiple Sclerosis Lesion Geometry in Quantitative Susceptibility Mapping (QSM) and Phase Imaging

Sarah Eskreis-Winkler, MD,¹ Kofi Deh, MS,¹ Ajay Gupta, MD,¹ Tian Liu, PhD,² Cynthia Wisnieff, BS,^{1,3} Moonsoo Jin, PhD,³ Susan A. Gauthier, MD,⁴ Yi Wang, PhD,^{1,3*} and Pascal Spincemille, PhD¹

Purpose: To demonstrate the phase and quantitative susceptibility mapping (QSM) patterns created by solid and shell spatial distributions of magnetic susceptibility in multiple sclerosis (MS) lesions.

Materials and Methods: Numerical simulations and experimental phantoms of solid- and shell-shaped magnetic susceptibility sources were used to generate magnitude, phase, and QSM images. Imaging of 20 consecutive MS patients was also reviewed for this Institutional Review Board (IRB)-approved MRI study to identify the appearance of solid and shell lesions on phase and QSM images.

Results: Solid and shell susceptibility sources were correctly reconstructed in QSM images, while the corresponding phase images depicted both geometries with shell-like patterns, making the underlying susceptibility distribution difficult to determine using phase alone. In MS patients, of the 60 largest lesions identified on T_2 , 30 lesions were detected on both QSM and phase, of which 83% were solid and 17% were shells on QSM, and of which 30% were solid and 70% were shell on phase. Of the 21 shell-like lesions on phase, 76% appeared solid on QSM, 24% appeared shell on QSM. Of the five shell-like lesions on QSM, all were shell-like on phase.

Conclusion: QSM accurately depicts both solid and shell patterns of magnetic susceptibility, while phase imaging fails to distinguish them.

Key Words: quantitative susceptibility mapping; multiple sclerosis; phase; iron

J. Magn. Reson. Imaging 2014;00:000-000.

© 2014 Wiley Periodicals, Inc.

MAGNETIC RESONANCE IMAGING (MRI) is routinely used to diagnose and monitor multiple sclerosis (MS) patients. Yet white matter lesions seen on conventional MRI sequences correlate only weakly with clinical disability score and are unable to convey the heterogeneous pathology found in MS lesions (1,2). More recently, gradient echo (GRE) MRI has been used to study demyelination (3,4) and iron distribution in multiple sclerosis (MS) lesions (5–8), which both contribute to changes in magnetic susceptibility. As such, the magnetic susceptibility distribution in MS lesions may be useful in monitoring disease progression (4,9).

Typically, GRE data are analyzed using $R2^*$, high-pass-filtered (HPF) phase imaging, and SWI (6,10–14). However, phase, which is well recognized to show dipole field effects (15), and $R2^*$, which approximately represents the field variation in a voxel, contains contributions from magnetic sources located in the surrounding voxels, making it difficult to interpret a lesion's magnetic susceptibility.

In phase imaging, "nodular" and "ring-like" MS lesions have been described (5,10,12). However, according to Maxwell's equations of electromagnetism (16), both solid (nodules) and shell (rings in 2D section) distributions of magnetic susceptibility can lead to shell-like patterns in phase-based images. This raises concerns about the reliability of phase-based imaging to detect these geometric susceptibility patterns in MS lesions.

Quantitative susceptibility mapping (QSM), which deconvolves the phase images, directly depicts the underlying magnetic susceptibility sources and may more accurately resolve the susceptibility spatial pattern in MS lesions (17). Given recent evidence that the geometry of MS lesions on susceptibility imaging can help identify clinically relevant lesion features (5), our purpose was to investigate differences in the depiction of solid and shell lesions in QSM and phase imaging.

MATERIALS AND METHODS

To characterize the appearance of solid and shell magnetic susceptibility sources on phase images and QSM, we performed numerical and experimental

¹Radiology Department, Weill Cornell Medical College, New York, NY, USA.

²Medimagetric, LLC, New York, NY, USA.

³Bioengineering Department, Cornell University, Ithaca, NY, USA.

⁴Neurology Department, Weill Cornell Medical College, New York, NY, USA.

Contract grant sponsor: National Institutes of Health (NIH); Contract grant numbers: R01EB013443 and R01NS072370.

*Address reprint requests to: Y.W., Weill Cornell Medical College, 515 East 71st St., Suite 104, New York, NY 10021.

E-mail: yiwang@med.cornell.edu

Received May 30, 2014; Accepted August 14, 2014.

DOI 10.1002/jmri.24745

View this article online at wileyonlinelibrary.com.

phantom validation, and then reviewed in vivo MS data. To evaluate MRI phase information, we used high-pass-filtered (HPF) phase images, the most commonly used phase technique (18).

Data Acquisition

Numerical Phantom

Magnitude, phase, and QSM images for a solid ball and spherical shell of magnetic susceptibility were generated using MatLab (MathWorks, Natick, MA). Three different sets of imaging parameters were used: isotropic parameters (matrix size: $128 \times 128 \times 128$; voxel size: $1 \times 1 \times 1$ mm), experimental phantom parameters (matrix size: $480 \times 64 \times 72$; voxel size: $0.5 \times 0.5 \times 0.5$ mm), and MS patient study parameters (matrix size: $512 \times 512 \times 50$, voxel size: $0.47 \times 0.47 \times 3$ mm). Other parameters were as follows: solid radius: 15 mm; shell outer/inner radius: 15/13 mm; field strength: 3T; $TE_1/\Delta TE$: 5/5 msec, 5 echoes, background/source magnetic susceptibility: 0.0/0.1 ppm) in a manner similar to previous work (19).

Experimental Phantom

For the solid lesion, a 50-mL plastic tube was filled halfway with 1% agarose and allowed to solidify. A 15-mm plastic ball was then placed on top of the agarose and additional agarose was added to completely cover the ball. The plastic ball was then extracted from the solidified agarose using a blade and tweezers, and 7.5 $\mu\text{g}/\text{mL}$ superparamagnetic iron oxide (SPIO) nanoparticles (20) with 1% agarose was injected in its place. The remainder of the tube was then filled with agarose and allowed to solidify.

To create the shell lesion, a 50-mL plastic tube was filled halfway with 1% agarose and allowed to solidify. A plastic ball was then placed on top of the agarose, was covered with more agarose, and then surgically removed as described above. Before filling the empty space with SPIO, a slightly smaller plastic ball was inserted in the empty space, and the SPIO nanoparticle/agarose mixture was injected surrounding the smaller ball to form a spherical shell of SPIO, which was then allowed to solidify. The smaller ball was then surgically removed and the shell center, as well as the rest of the tube, was subsequently filled with agarose.

Tubes were scanned using a 3D multiecho GRE sequence on a 3.0T scanner (GE Medical Systems, Milwaukee, WI) with a single-channel wrist coil (matrix size: $480 \times 64 \times 72$, voxel size: $0.5 \times 0.5 \times 0.5$ mm, 11 echoes, $TE_1/\Delta TE/\text{TR}$: 4.6/5/60 msec).

In Vivo MS Data

This retrospective study was approved by our Institutional Review Board (IRB). We reviewed the MRI database in our institution's clinical PACS system and identified 20 consecutive patients who met both of the following criteria: 1) clinically confirmed MS patients; 2) underwent an MR scan including a 3D multiple-echo GRE sequence (matrix size: $512 \times 512 \times 50$,

voxel size: $0.47 \times 0.47 \times 3$ mm, 11 echoes, $TE_1/\Delta TE/\text{TR}$: 4.5/4.8/57.9 msec) as part of the current standard-of-care at our institution between October 1, 2013 and October 20, 2013. MRI was performed on a 3.0T MRI system (SignaHDxt, GE).

All 20 patients (6 male, 14 female, age 32–69, 45.75 ± 10.44 years) were MS patients with expanded disability status scale ranging from 0 to 8 (median: 1.25) and disease duration ranging from 3 to 26 (10.65 ± 6.60) years. All patients in this study have been treated with a standard immunomodulatory therapy (including interferon beta 1a, glatiramer acetate, fingolimod, natalizumab, rituximab).

Data Analysis

For the numerical simulation, experimental phantom, and in vivo data, HPF phase images were generated using a 3D high-pass filter that was $12 \times 12 \times 12$ voxels (18). QSM images were reconstructed from the 3D multiecho GRE data as follows. A field map was generated by performing a voxel-by-voxel nonlinear least-squares fitting of the complex signal over TE. Next, the background field (ie, the magnetic field generated by susceptibility sources outside the region of interest) was removed by applying the Projection onto Dipole Fields (PDF) algorithm (21). Finally, the magnetic field-to-susceptibility-source inverse problem was solved using morphology enabled dipole inversion (MEDI), which uses a regularization term that promotes similarity of edges between the QSM and the magnitude image (17,22–24).

For the experimental phantom results, a neuroradiologist with 8 years of experience (A.G.) categorized the lesions on HPF phase and QSM as either "solid" or "shell."

For the in vivo MS cases, the neuroradiologist first identified the three largest separate lesions on T_2 -weighted images based on visible hyperintensity. He then characterized the morphology of each lesion as "solid," "shell," or "not seen" on the HPF phase and QSM images. To reduce the risk of bias, the neuroradiologist classified MS lesions on the HPF phase and QSM images in two different sessions separated by several weeks.

If a lesion was visualized on phase but not on QSM, neighboring slices were examined to investigate whether the signal on phase was really the magnetic field generated by a nearby susceptibility source, rather than being a manifestation of the MS lesion seen on T_2 .

Statistical Analysis

For the solid and shell numerical simulations, a Pearson's correlation coefficient was calculated between the middle axial slice of true lesion and the QSM reconstruction, as well as between the middle axial slice true lesion and the HPF phase reconstruction.

For the phantom and MS data, the percentage of HPF phase and QSM lesions designated as solid and shell by the neuroradiologist were calculated and compared.

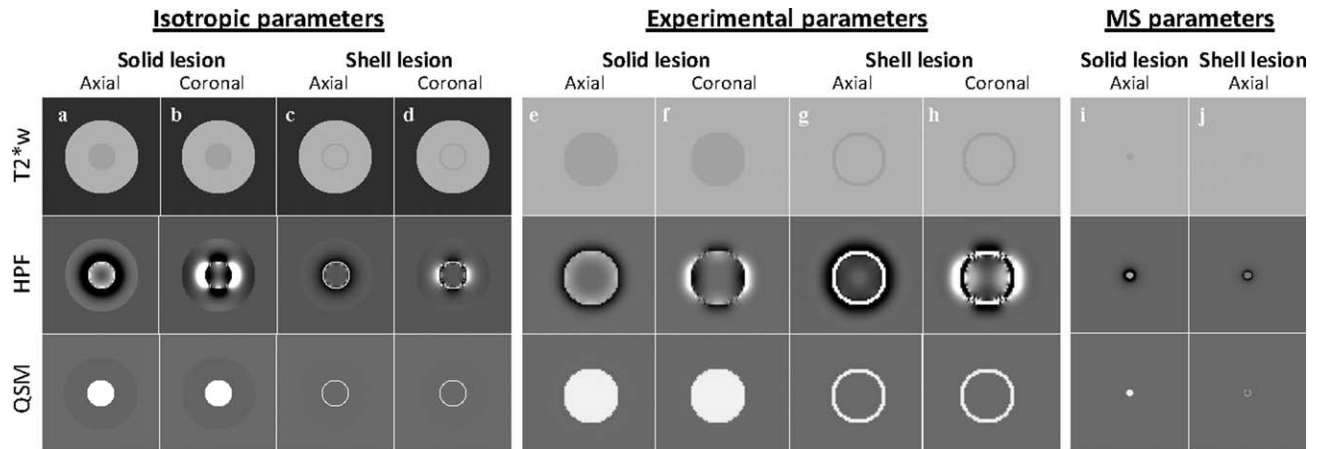


Figure 1. Numerical simulations of solid and shell lesions using isotropic, experimental phantom, and MS patient study parameters. For the solid lesions, (a,e,i) show T_2^* -weighted, HPF phase, and QSM images in axial view with corresponding coronal sections in (b,f). For the shell lesions, (c,g,j) show T_2^* -weighted, HPF phase, and QSM images in axial view with corresponding coronal sections in (d,h). Coronals are not shown for MS patient parameter simulations since MS patient data was analyzed in axial view only).

RESULTS

The results of the numerical simulations are shown in Fig. 1. The Pearson's correlation coefficients between the true solid and shell lesions and their respective QSM reconstructions were greater than 0.99. The correlation coefficient between the true shell lesion and its HPF phase image was 0.91, and the correlation coefficient between the solid lesion and its HPF phase image was 0.49. This demonstrates that shell lesions are accurately depicted on both phase and QSM, while solid lesions are more accurately depicted on QSM than on phase.

The results of the SPIO phantom experiments are shown in Fig. 2. The neuroradiologist, blinded to true lesion geometry, correctly identified the solid and shell lesions on QSM images, but labeled both the solid and shell lesions as "shell-like" on HPF phase images. Therefore, on phase images both solid and shell sources of magnetic susceptibility appeared shell-like and were difficult to distinguish. The QSM images correctly depicted the underlying geometry, thus enabling the differentiation of solid and shell sources of magnetic susceptibility.

Of the 60 lesions identified in the 20 MS subjects in the T_2 -weighted images, 30 lesions were detected on both phase and QSM, of which 25 (83%) were solids and 5 (17%) were shells on QSM, and of which 9 (30%) were solids and 21 (70%) were shells on phase. Table 1 presents the morphological characteristics of all lesions on phase and QSM. The long axis of the lesions ranged from 0.23–2.1 cm (5–45 voxels). Representative lesion images are shown in Fig. 3. Of the nine lesions that appeared solid on phase, 100% appeared as solid on QSM. Of the 21 lesions that appeared as shells on phase, 16 (76%) appeared as solid on QSM, and five (24%) appeared as shell on QSM. Of the five lesions that appeared as shells on QSM, all five (100%) appeared as shells on phase.

For the two MS lesions that were identified on phase but not on QSM, examination of neighboring QSM slices revealed the presence of veins, suggesting that the

shell-like structures identified on HPF phase could be a manifestation of the magnetic field generated by the nearby venous susceptibility sources, rather than being a manifestation of the lesions seen on T_2 at that location (Fig. 4).

DISCUSSION

Our results indicate that QSM can more accurately distinguish between solid and shell patterns of magnetic susceptibility compared to phase imaging. Shell-shaped lesions on phase can result from either solid or shell susceptibility sources. These results are consistent with the physics theory, and suggest that QSM better depicts spatial susceptibility patterns in MS lesions compared to phase-based imaging.

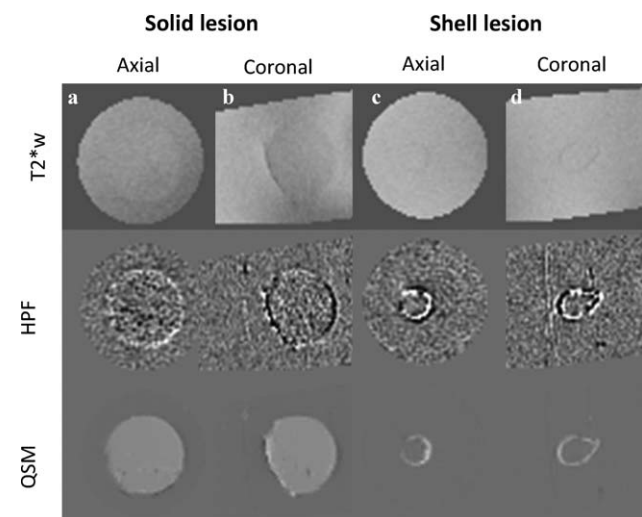


Figure 2. SPIO solid and shell phantom lesions. (a) T_2^* -weighted, HPF phase, and QSM images of solid lesion in axial view with corresponding coronal sections in (b); (c) T_2^* -weighted, HPF phase, and QSM images of shell lesion in axial view with corresponding coronal sections in (d).

Table 1
Morphological Characteristics of the 60 MS Lesions Identified on T_2 -Weighted Images

Phase	QSM	No. of lesions
Shell	Shell	5
Shell	Solid	16
Solid	Solid	9
Not visible	Not visible	15
Shell	Not visible	2
Solid	Not visible	1
Not visible	Shell	2
Not visible	Solid	10

Conventional MRI sequences can identify white matter lesions, but reveal little about underlying pathophysiological processes, such as iron deposition, macrophage/microglia activation patterns, and demyelination (1). A lesion's magnetic susceptibility distribution signature, however, may contain this clinically useful information, and could potentially be used both to distinguish different pathological stages of lesion genesis as well as to investigate factors that influence overall recovery of an MS lesion (2,3). For instance, a shell-shaped susceptibility distribution may signify the presence of iron-containing macrophages at the rim of a chronic active lesion (5–7,25). A solid-shaped susceptibility distribution, depending on its magnetic susceptibility value, could denote either extensive demyelination (and lack of iron) as found in chronic, inactive lesions (25), or could represent the

uniform distribution of cellular or extracellular sources of iron (7). Further investigation is needed to refine our understanding of the relationship between lesion susceptibility geometry and the pathological significance, but early studies already highlight the importance of differentiating between solid and shell lesion geometries.

The veins identified on slices adjacent to the two MS lesions that were shell-like on phase but not visible on QSM underscores that shell-like structures on HPF phase may represent the magnetic field generated by nearby veins, rather than being manifestations of the tissue at that point in space. These HPF "false positives" further highlight the pitfalls of using phase imaging, which depicts the magnetic field generated by nearby susceptibility sources, rather than QSM, which depicts the geometry of the susceptibility sources themselves. T_2 lesions not detected on QSM are likely old (>7 years) chronic lesions (9).

According to the Maxwell's equations, each source of magnetic susceptibility generates a magnetic field that changes rapidly in the vicinity of that source and extends beyond it (16). The phase of an MR image is proportional to this magnetic field. The large changes in the magnetic field in the vicinity of the source create the shell-like artifacts demonstrated in the phase images of the numerical simulations and phantom experiments.

A few limitations should be considered. First, our study lacked histological correlates for the MS patient data; "ground truth" geometries were not available for

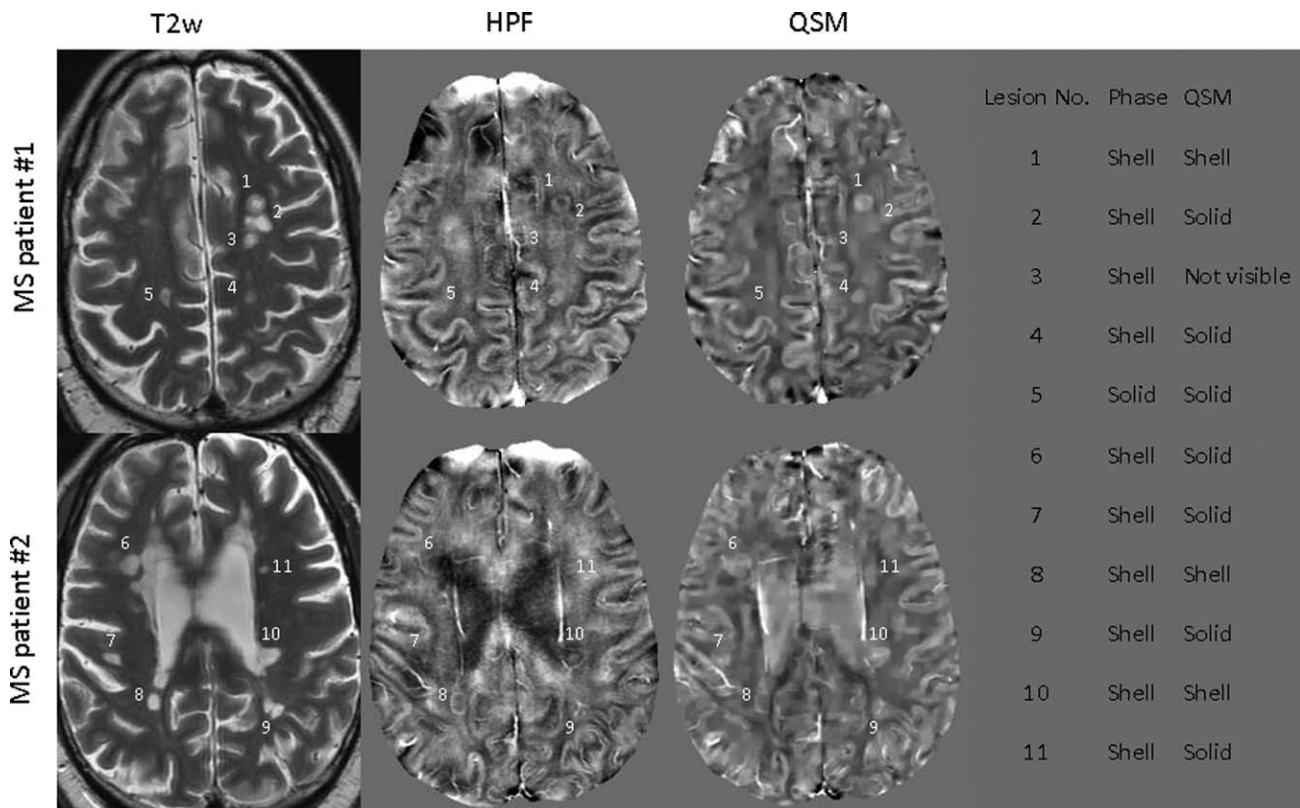


Figure 3. Representative lesions in two MS patients demonstrate that shell appearance on HPF phase imaging can correspond to either solid (eg, lesion 4) or shell (eg, lesion 8) on QSM. On the right, lesions visible on T_2 w are numbered and their geometrical appearances on HPF phase and QSM are listed.

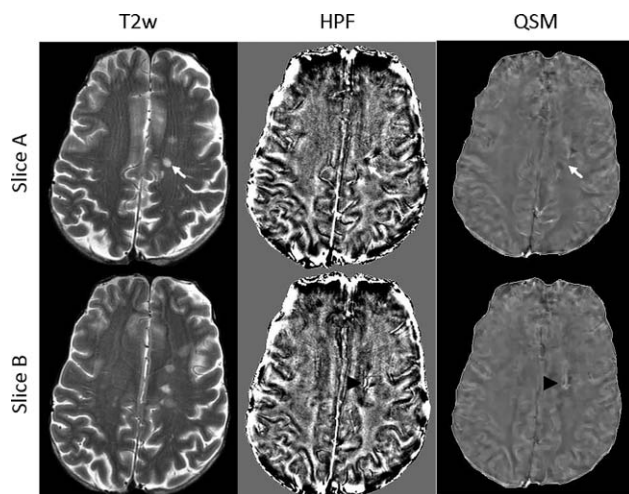


Figure 4. Veins adjacent to MS lesions may cause nonlocal signal changes on HPF phase, complicating the interpretation of MS lesion-generated signal. For instance, the MS lesion identified on slice A of T_2w (white arrow) appears shell-like on HPF phase but is not visible on QSM. However, inspection of neighboring slice B reveals an adjacent vein on HPF phase and QSM (black arrowhead) which may have generated the HPF phase signal change on slice A.

our *in vivo* analysis. The physics of magnetic susceptibility and field is well established by Maxwell's equations, which lends support for the interpretation of our *in vivo* data. Second, the 3 mm slice thickness of the MS data did not permit examination of very small lesions, which may have different phase behavior due to averaging. These very small lesions, which could indicate new disease activity, are an important area of future study. Still, a wide range of lesion sizes were evaluated. Some subjects had larger lesions than others, and so by choosing the three largest lesions in each subject, lesion sizes ranged from 0.23 to 2.1 cm. Third, the classification of spatial distribution patterns into either solids or shell shapes on MRI may be subject to interpretive differences between readers. Thus, future studies should assess interobserver variability in interpretation, especially as future work elucidates the significance of shell and solid susceptibility geometries in the pathophysiology of MS lesions. Fourth, it is important to note that a QSM voxel reports the sum of all enclosed susceptibility sources, which, in our clinical cases, includes not only paramagnetic iron but diamagnetic myelin as well. To isolate the iron content of MS lesions, the myelin contribution must be removed using, for example, myelin mapping (26,27) or ultrashort TE imaging (28–30).

However, it is important to note that only a subset of MS lesions visible on T_2 were seen on phase or QSM. This is consistent with previous literature (9), which has found that very early active and old chronic inactive MS lesions often lack susceptibility-based contrast and are not visible on phase or QSM.

In conclusion, QSM can discriminate between solid and shell patterns of magnetic susceptibility with greater accuracy than phase imaging. Given evidence of the importance of susceptibility geometry in charac-

terizing clinically relevant characteristics of MS lesions, QSM should be included in future MRI studies of susceptibility in MS.

REFERENCES

- Poloni G, Minagar A, Haacke EM, Zivadinov R. Recent developments in imaging of multiple sclerosis. *Neurologist* [Internet]. 2011 Jul [cited 2014 Apr 11];17:185–204. Available from: <http://www.ncbi.nlm.nih.gov/pubmed/21712664>
- Zivadinov R, Leist TP. Clinical-magnetic resonance imaging correlations in multiple sclerosis. *J Neuroimaging* [Internet]. 2005 Jan [cited 2014 Apr 11];15(4 Suppl):10S–21S. Available from: <http://www.ncbi.nlm.nih.gov/pubmed/16385015>
- Yablonskiy DA, Luo J, Sukstanskii AL, Iyer A, Cross AH. Biophysical mechanisms of MRI signal frequency contrast in multiple sclerosis. *Proc Natl Acad Sci U S A* [Internet]. 2012 Aug 28 [cited 2014 Apr 2];109:14212–14217. Available from: <http://www.pubmedcentral.nih.gov/articlerender.fcgi?artid=3435153&tool=pmcentrez&rendertype=abstract>
- Wiggermann V, Hernández Torres E, Vavasour IM, et al. Magnetic resonance frequency shifts during acute MS lesion formation. *Neurology* [Internet]. 2013 Jul 16 [cited 2014 Apr 8];81:211–218. Available from: <http://www.pubmedcentral.nih.gov/articlerender.fcgi?artid=3770162&tool=pmcentrez&rendertype=abstract>
- Mehta V, Pei W, Yang G, et al. Iron is a sensitive biomarker for inflammation in multiple sclerosis lesions. *PLoS One* [Internet]. 2013 Jan [cited 2013 Dec 10];8:e57573. Available from: <http://www.pubmedcentral.nih.gov/articlerender.fcgi?artid=3597727&tool=pmcentrez&rendertype=abstract>
- Bagnato F, Hametner S, Yao B, et al. Tracking iron in multiple sclerosis: a combined imaging and histopathological study at 7 Tesla. *Brain* [Internet]. 2011 Dec [cited 2013 Nov 11];134(Pt 12):3602–3615. Available from: <http://www.pubmedcentral.nih.gov/articlerender.fcgi?artid=3235560&tool=pmcentrez&rendertype=abstract>
- Hametner S, Wimmer I, Haider L, Pfeifenbring S, Brück W, Lassmann H. Iron and neurodegeneration in the multiple sclerosis brain. *Ann Neurol* [Internet]. 2013 Jul 19 [cited 2013 Nov 18]; Available from: <http://www.ncbi.nlm.nih.gov/pubmed/23868451>
- Bagnato F, Hametner S, Welch EB. Visualizing iron in multiple sclerosis. *Magn Reson Imaging* [Internet]. 2013 Apr [cited 2013 Dec 2];31:376–384. Available from: <http://www.ncbi.nlm.nih.gov/pubmed/23347601>
- Chen W, Gauthier SA, Gupta A, et al. Quantitative susceptibility mapping of multiple sclerosis lesions at various ages. *Radiology* [Internet]. 2014 Apr [cited 2014 Mar 27];271:183–192. Available from: <http://www.ncbi.nlm.nih.gov/pubmed/24475808>
- Bian W, Harter K, Hammond-Rosenbluth KE, et al. A serial *in vivo* 7T magnetic resonance phase imaging study of white matter lesions in multiple sclerosis. *Mult Scler* [Internet]. 2013 Jan [cited 2013 Dec 10];19:69–75. Available from: <http://www.ncbi.nlm.nih.gov/pubmed/22641301>
- Deistung A, Schäfer A, Schweser F, Biedermann U, Turner R, Reichenbach JR. Toward *in vivo* histology: a comparison of quantitative susceptibility mapping (QSM) with magnitude-, phase-, and R_2^* -imaging at ultra-high magnetic field strength. *Neuroimage* [Internet]. 2013 Jan 15 [cited 2013 Nov 7];65:299–314. Available from: <http://www.ncbi.nlm.nih.gov/pubmed/23036448>
- Haacke EM, Makki M, Ge Y, et al. Characterizing iron deposition in multiple sclerosis lesions using susceptibility weighted imaging. *J Magn Reson Imaging* [Internet]. 2009 Mar [cited 2013 Dec 8];29:537–544. Available from: <http://www.pubmedcentral.nih.gov/articlerender.fcgi?artid=2650739&tool=pmcentrez&rendertype=abstract>
- Hagemeyer J, Heininen-Brown M, Poloni GU, et al. Iron deposition in multiple sclerosis lesions measured by susceptibility-weighted imaging filtered phase: a case control study. *J Magn Reson Imaging* [Internet]. 2012 Jul [cited 2013 Dec 10];36:73–83. Available from: <http://www.ncbi.nlm.nih.gov/pubmed/22407571>
- Walsh AJ, Lebel RM, Eissa A, et al. Multiple sclerosis: validation of MR imaging for quantification and detection of iron. *Radiology* [Internet]. 2013 May [cited 2013 Dec 10];267:531–542. Available from: <http://www.ncbi.nlm.nih.gov/pubmed/23297322>
- Haacke EM, Brown RW, Thompson MR, Venkatesan R. *Magnetic resonance imaging: physical principles and sequence design*. New York: John Wiley & Sons; 1999.
- Jackson J. *Classical electrodynamics*, 3rd ed. New York: John Wiley & Sons; 1998.

17. Liu T, Wisnieff C, Lou M, Chen W, Spincemaille P, Wang Y. Non-linear formulation of the magnetic field to source relationship for robust quantitative susceptibility mapping. *Magn Reson Med* [Internet]. 2013 Feb [cited 2013 Nov 8];69:467–476. Available from: <http://www.ncbi.nlm.nih.gov/pubmed/22488774>
18. Wang Y, Yu Y, Li D, et al. Artery and vein separation using susceptibility-dependent phase in contrast-enhanced MRA. *J Magn Reson Imaging* [Internet]. 2000 Nov [cited 2014 Apr 9];12:661–670. Available from: <http://www.ncbi.nlm.nih.gov/pubmed/11050635>
19. Salomir R, de Senneville BD, Moonen CT. A fast calculation method for magnetic field inhomogeneity due to an arbitrary distribution of bulk susceptibility. *Concepts Magn Reson* [Internet]. 2003 Oct 13 [cited 2014 May 29];19B:26–34. Available from: <http://doi.wiley.com/10.1002/cmr.b.10083>.
20. Wong R, Chen X, Wang Y, Hu X, Jin MM. Visualizing and quantifying acute inflammation using ICAM-1 specific nanoparticles and MRI quantitative susceptibility mapping. *Ann Biomed Eng* [Internet]. 2012 Jun [cited 2013 Dec 9];40:1328–1338. Available from: <http://www.ncbi.nlm.nih.gov/pubmed/22143599>.
21. Liu T, Khalidov I, de Rochefort L, et al. A novel background field removal method for MRI using projection onto dipole fields (PDF). *NMR Biomed* [Internet]. 2011 Nov [cited 2014 Feb 22];24:1129–1136. Available from: <http://www.pubmedcentral.nih.gov/articlerender.fcgi?artid=3628923&tool=pmcentrez&rendertype=abstract>
22. Kressler B, de Rochefort L, Liu T, Spincemaille P, Jiang Q, Wang Y. Nonlinear regularization for per voxel estimation of magnetic susceptibility distributions from MRI field maps. *IEEE Trans Med Imaging* [Internet]. 2010 Mar [cited 2014 May 30];29:273–281. Available from: <http://www.pubmedcentral.nih.gov/articlerender.fcgi?artid=2874210&tool=pmcentrez&rendertype=abstract>
23. De Rochefort L, Liu T, Kressler B, et al. Quantitative susceptibility map reconstruction from MR phase data using bayesian regularization: validation and application to brain imaging. *Magn Reson Med* [Internet]. 2010 Jan [cited 2014 May 30];63:194–206. Available from: <http://www.ncbi.nlm.nih.gov/pubmed/19953507>.
24. Liu J, Liu T, de Rochefort L, et al. Morphology enabled dipole inversion for quantitative susceptibility mapping using structural consistency between the magnitude image and the susceptibility map. *Neuroimage* [Internet]. 2012 Mar 1 [cited 2014 May 30];59:2560–2568. Available from: <http://www.pubmedcentral.nih.gov/articlerender.fcgi?artid=3254812&tool=pmcentrez&rendertype=abstract>
25. Lassmann H. Review: the architecture of inflammatory demyelinating lesions: implications for studies on pathogenesis. *Neuropathol Appl Neurobiol* [Internet]. 2011 Dec [cited 2014 Apr 11];37:698–710. Available from: <http://www.ncbi.nlm.nih.gov/pubmed/21696413>.
26. Shen X, Nguyen TD, Gauthier SA, Raj A. Robust myelin quantitative imaging from multi-echo T2 MRI using edge preserving spatial priors. *Med Image Comput Assist Interv* [Internet]. 2013 Jan [cited 2014 Apr 9];16(Pt 1):622–630. Available from: <http://www.ncbi.nlm.nih.gov/pubmed/24505719>.
27. Nguyen TD, Wisnieff C, Cooper MA, et al. T2 prep three-dimensional spiral imaging with efficient whole brain coverage for myelin water quantification at 1.5 Tesla. *Magn Reson Med* [Internet]. 2012 Mar [cited 2014 Apr 9];67:614–621. Available from: <http://www.ncbi.nlm.nih.gov/pubmed/22344579>.
28. Du J, Ma G, Li S, et al. Ultrashort echo time (UTE) magnetic resonance imaging of the short T2 components in white matter of the brain using a clinical 3T scanner. *Neuroimage* [Internet]. 2014 Feb 15 [cited 2014 Apr 1];87:32–41. Available from: <http://www.ncbi.nlm.nih.gov/pubmed/24188809>.
29. Horch RA, Gore JC, Does MD. Origins of the ultrashort-T2 1H NMR signals in myelinated nerve: a direct measure of myelin content? *Magn Reson Med* [Internet]. 2011 Jul [cited 2014 Apr 9];66:24–31. Available from: <http://www.pubmedcentral.nih.gov/articlerender.fcgi?artid=3120910&tool=pmcentrez&rendertype=abstract>
30. Wilhelm MJ, Ong HH, Wehrli SL, et al. Direct magnetic resonance detection of myelin and prospects for quantitative imaging of myelin density. *Proc Natl Acad Sci U S A* [Internet]. 2012 Jun 12 [cited 2014 Apr 9];109:9605–9610. Available from: <http://www.pubmedcentral.nih.gov/articlerender.fcgi?artid=3386098&tool=pmcentrez&rendertype=abstract>